Progress In Electromagnetics Research B, Vol. 95, 81–101, 2022

3D Transient Nonlinear Magneto-Thermal Analytical Model Calculation in PM Induction Heating Device

Abdi Ammar[1, *], Youcef Ouazir[1], Georges Barakat[2], and Yacine Amara[2]

Abstract—This paper aims to develop a new 3D analytical model devoted to the study of nonlinear transient magneto-thermal coupled problems in permanent magnet transverse flux induction heating device (PMTFIHD). Firstly, a 3D analytical solution of magneto-dynamic field problem taking into account the transverse edge effect in the workpiece is derived using variables' separation technique. This transverse edge effect allows determining the exact resulting heating power density, which is the heat source of the transient thermal problem in the work-piece. Secondly, the 3D transient analytical solution of the temperature distribution is obtained by combining variables' separation technique and Green's function method. Then, the previous models are exploited in a transient simulations procedure of the magneto-thermal process allowing the nonlinear physical properties of the part to be taking into account. Finally, the performances of the studied PMTFIHD will be calculated, in order to validate the developed 3D coupled models. The simulation results from the developed models are validated with those obtained by the finite element method and the experimental results.

1. INTRODUCTION

Magnetic induction and magneto-thermal are themselves a real future solution for industrial applications of induction heating. Modern topologies are not simple copies of conventional heating [1]. The development of new topologies based on inductors with permanent magnets [2–4] or HTS coils [5–7] is one of the future challenges worldwide, when the gain in yield and/or in operating mode becomes essential (surface treatment, core heating at heart ...). Induction heating is currently used in many metallurgical processes. In addition, one of the specific industrial applications is the high strength application indicated in aerospace and transportation industries that refers to the process of pressing aluminum (billets or plates) [8]. In this application, the workpiece (billet, plate) is preheated to a uniformly distributed temperature of about 400°C (total aluminum expansion temperature) before being placed in the forming press. Two technological solutions are used to carry out this heating process of non-magnetic parts. First, conventional heaters (winding powered by alternating current) are used [9]. The major drawback of this technique is its low efficiency, which is about 50% [10]. The second consists in moving the part inside a strong constant magnetic field, created by HTS coils [10], and a yield above 90% is theoretically proven [11], but this technology is very expensive. More recently, [2, 4, 12, 13] have proposed a new concept of induction heating using modern permanent magnets instead of HTS. The efficiency of this heating is about 85% [2].

In general, the study of induction heating devices requires effective multi-physics modeling, which involves coupled magneto-thermal phenomena [14–16]. This step is very complex because of the interdependence between the different parameters, which makes the overall behavior of this process

Received 6 January 2022, Accepted 14 April 2022, Scheduled 26 April 2022

* Corresponding author: Abdi Ammar (aabdi@usthb.dz).

[1] Electrical and Industrial Systems Laboratory (LSEI), University of Science and Technology (USTHB), BP N°32 El Alia Bab Ezzouar, Algiers, Algeria. [2] Electrical Engineering and Automation Research Group, GREAH University of Havre France, GREAH, EA3220 le Havre 76600, France.

difficult to apprehend. Indeed, the heat transfer prediction and temperature distribution in electrical devices are realized by using the finite element method [17–20] and/or thermal equivalent circuit [21–23]; the analytical resolution of partial differential equations representing the temperature distribution in electrical machines does not exist [24]. However, the simultaneous numerical solution of the Maxwell and Fourier equations overtime is not an effective approach, as it requires significant computational time due to the discrepancy between the constant rates of thermal and electrical time as well as the complexity of the mathematical equations.

In this work, we present a new 3-D analytical coupling method between the two phenomena; the magneto-thermal process is systematically evaluated over time. In [8], we have developed a 2D magneto-dynamic analytic model to compute the heating power in the conductive plate of a novel translational motion heating device shown in Figure 1; this model is not suitable for the device studied which has strong edge effects. First, in order to take into account the transverse edge effect, in [25] the 2D developed model is extended to a 3D analytical model by taking the transverse edge effect in a very similar manner to [26, 27], and a correction factor is defined.

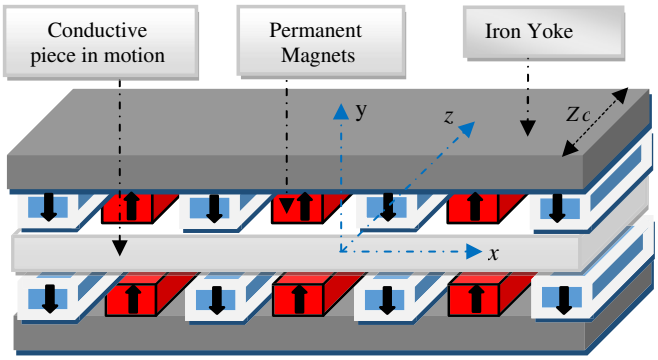

Figure 1. 3D induction heater geometry with permanent magnets.

Purely 3-D models are less common because they are more complex to implement [28–30], but this type of modelling allows for accurate results that are very close to reality [31–37]. In this and other context, to improve the accuracy of 3D results, an accurate 3D electromagnetic model to compute heating power is proposed in the present paper. Then, a purely analytical expression for the evaluation of induced heating power is derived from the 3D solution. The latter, which depends directly on the physical and geometric parameters, is obtained by solving the Maxwell PDE in 3D Cartesian coordinates. All 2D, 2D/extended-3D and 3D magnetic models are compared to 3D finite element simulations in order to highlight the effect of the transverse finite length on the thermal power density.

Secondly, a 3D transient thermal model, based on a synergy between the variables separation technique and the Green functions in transient regime, is developed. Then, the magneto-thermal model is obtained by a strong coupling between a 3D magnetic and transient thermal models, taking into account the variation of electrical and thermal physical properties of the workpiece.

Finally, the comparison of the results obtained by this model of coupling related to the spatio-temporal evolution of the temperature in the workpiece with those resulting from 3D finite element computations and experimental results has highlighted the validity of the approach that we proposed.

2. 3D AND 2D MAGNETIC ANALYTICAL MODELS

2.1. Geometry Description of the PM Induction Heater

It concerns a new transverse flux PM induction heating device, in which the part to be heated is a parallelepipedal conductive plate placed inside a double permanent magnet inductor and subjected to a linear movement. The displacement of the workpiece in the static magnetic field generates induced currents that produce the necessary heating power. In this device, a low linear velocity is recommended to reach a large skin depth as to obtain a homogeneous distribution of the heating power and temperature.

The physical proprieties and geometrical dimensions of the studied induction heater are shown in Table 1.

Table 1. Physical and geometrical parameters of the studied induction heater.

Symbol	Quantity	Value
$2 * y_1$	Workpiece thickness	15 mm
e	Air-gap thickness	3 mm
b	Permanent magnets thickness	10 mm
z_a	Permanent magnets length	50 mm
a	Permanent magnets width	40 mm
e_g	Distance between two magnets	4 mm
Z_p	Width workpiece	50 mm
L	Workpiece Length	400 mm
y_c	Iron yoke thickness	20 mm
Z_c	Iron yoke width	50 mm
V	Speed of translation	Variable m/s
λ	Thermal conductivity at T_0	$206\,\mathrm{w}\cdot\mathrm{m}^{-1}\cdot\mathrm{K}^{-1}$
C_p	Specific heat at T_0	$936\,\mathrm{J}\cdot\mathrm{kg}^{-1}\cdot\mathrm{K}^{-1}$
B_r	Remanent flux density of magnet	1.2 T
ρ	Aliminum density	$2700\,\mathrm{kg/m}^3$
σ	Electrical conductivity at T_0	$37\times10^6\ (\Omega\cdot\mathrm{m})^{-1}$
α	Aluminium thermal coefficient	$3.9\times10^{-3}\,\mathrm{K}^{-1}$

2.2. 2D Magnetic Model and Extended 2D/3D Magnetic Model

The 2D geometrical model shown in Figure 2 is used in [8] where the electromagnetic problem is formulated with a magnetic vector potential $\vec{A}$. The electromagnetic behavior of the studied system is governed by:

$$\Delta\vec{A} = -\mu\sigma(\vec{v}\wedge r\vec{o}t\vec{A}) - r\vec{o}t\vec{M} \tag{1}$$

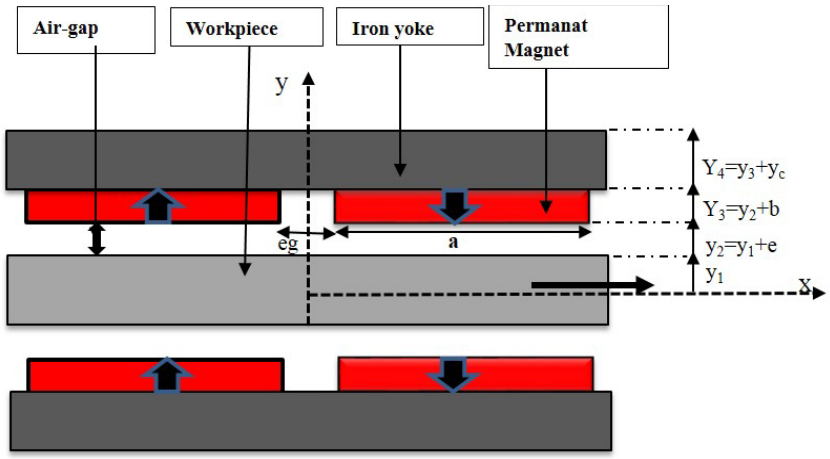

Figure 2. 2D induction heater geometry in X-Y plane.

All 2D analytical magnetic model details are illustrated in [8]; remember that the resulting power loss density using the 2D model is given as following:

$$p\,(x,y)) = \frac{1}{\sigma}(J_{ind}(x,y))^2 \tag{2}$$

The total heating power is evaluated by integrating Eq. (2) on the workpiece volume:

$$P_T = z_p \cdot \iint_S p\,(x,y)\,dxdy \tag{3}$$

The induced heating power density calculation using the 2D developed magnetodynamic model has a lack of accuracy due to the non-consideration of the eddy currents flowing in the x-direction. Then, in order to take into account the edge effect along z direction, the 2D model is extended to 3D using the same method as in [27] (Figure 3).

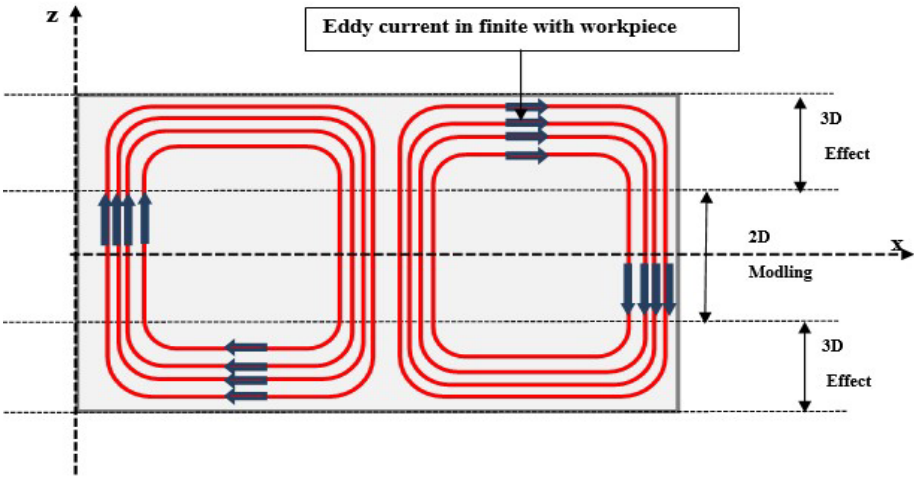

Figure 3. Eddy current distribution with 3D effect.

All details of model 2D-Extended 3D are illustrated in [25]; remember that the resulting power loss density using the extended model 2D-3D is obtained as:

$$p_{cor}\,(x,y,z) = \frac{1}{\sigma}(J_x(x,y)^2 + J_z(x,y)^2) \tag{4}$$

Therefore, the total heating power defined by Eq. (3) will be defined as integrating Eq. (4) on the workpiece volume, and we have acquired:

$$P_{TC} = K_{corr} P_T \tag{5}$$

where K_{corr} is a coefficient that corrects the distribution of the induced currents density in the parallelepiped workpiece. It is expressed as follows:

$$K_{corr}(n) = 1 - \frac{\tau}{n\pi Z_p} \tanh\left(\frac{n\pi Z_p}{\tau}\right) \tag{6}$$

2.3. 3D Magnetic Analytic Model

We first consider an area of resolution of air, iron, and permanent magnets of the lower inductor (the magnets of the upper inductor are off) (Figure 4), then we calculate the magnetic field using a magnetic field formulation of scalar potential. This assumes that the conductive part has no effect on the magnetic problem; the magnetic reaction of the currents induced in the workpiece is not taken into account in this model. This assumption is justified by the fact that the speed of translation of the part must be

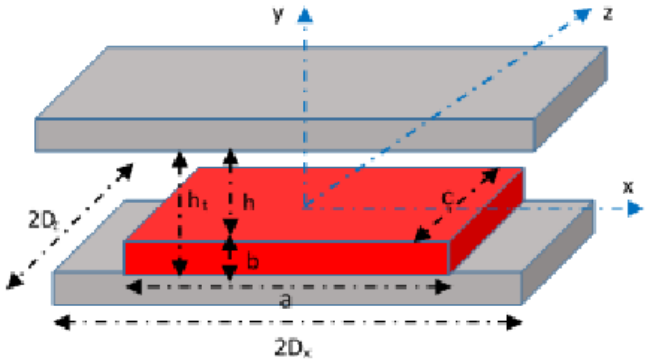

Figure 4. 3D dimensions of one magnet pole.

low to have a uniform heating [25]. We also consider an infinite permeability of the iron yokes. Hence, the magnetic field is null in the iron parts. The boundary condition on the iron interface is then:

$$\vec{n} \wedge \vec{H} = 0 \tag{7}$$

Vector $\vec{n}$ is the outgoing normal to the surface considered (plane x-z) and $\vec{H}$ the magnetic field. Rare-earth permanent magnets have a relative permeability close to that of air (NdFeB, $\mu_r = 1$).

Under the hypotheses mentioned above, the magnetic problem treated is of the magneto-static type and very suitable for a formulation in scalar potential (U), in different media of the geometrical model shown in Figure 5, and the magnetic flux density is calculated by:

$$\begin{cases} \vec{H} = -g\vec{r}adU \\ \Delta U = div\vec{M} \quad \text{Magnets Region I} \\ \Delta U = 0 \quad \text{Air Region II} \end{cases} \tag{8}$$

where $\vec{M}$ is the magnetization of the permanent magnets.

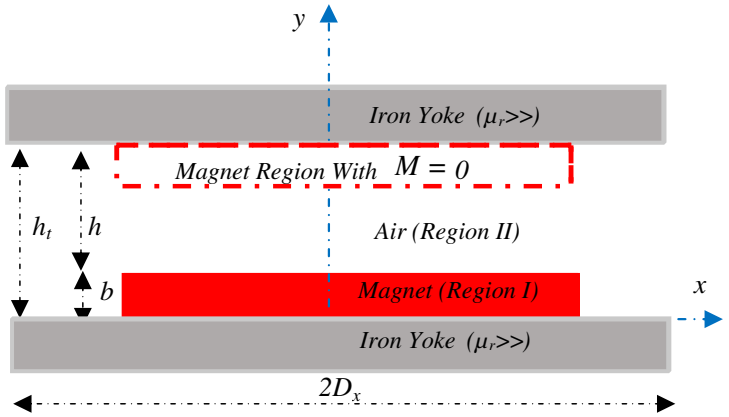

Figure 5. Geometrical model in the plane (x-y).

To solve the system of Equation (8), border conditions must be imposed:

- The condition in $x = \pm D_x$ is naturally anti-periodic. We find this condition physically in the device along the x-axis where we see an alternating polarity of the magnetic poles. This condition is expressed mathematically in the case of a resolution in scalar potential by:

$$U(-D_x) = -U(D_x) \tag{9}$$

- Along the y axis, the boundaries of the problem stop at the level of the ferromagnetic yokes, where the conditions represented by Equation (7) have already been imposed.

- At the border $z = \pm D_z$ we use anti-periodicity condition, while respecting D_z (half length of the system along z) very large in front of $c/2$ (active length along z); we pose $D_z = c$; this condition leads to $\vec{B} = 0$ at $z = \pm D_z$.

$$U(-D_z) = -U(D_z) \tag{10}$$

As stated above the whole resolution domain contains magnet and air regions. Figure 5 illustrates the geometric model in the plane (x-y). The first (region I) includes the sources of the magnetic field (magnetization $\vec{M}$) for the permanent magnets placed in $y \in [0, b]$. The second region has air placed in $y \in [b, h]$.

The studied problem has as a magnetic field source a permanent magnet with a homogeneous magnetization oriented along the axis y. After decomposition into double Fourier series along x- and z-directions (see Figure 6), the magnetization vector can be put in the form:

$$\vec{M} = M_y(x, z)\vec{u}_y \tag{11}$$

$$M_y(x, z) = \sum_{n=1}^{\infty} \sum_{m=1}^{\infty} M_{nm} \cos(W_n x) \cos(W_m z) \tag{12}$$

with:

$$\begin{cases} M_{nm} = \dfrac{16 B_r}{\mu_0 nm\pi^2} \sin(W_n a/2) \sin(W_m c/2) \\ W_n = \dfrac{n\pi}{2D_x}; \quad W_m = \dfrac{m\pi}{2D_z} \end{cases} \qquad n, m = 1, 3, 5, \ldots$$

Note that n and m are odd integers, and B_r is the residual flux density of the permanent magnets.

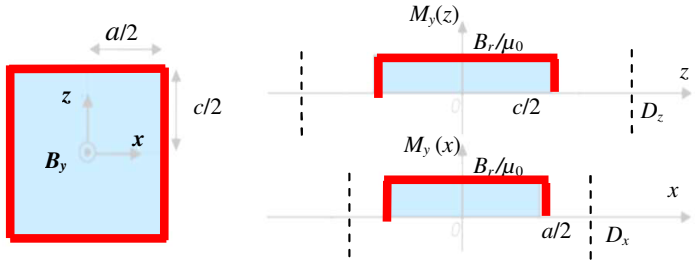

Figure 6. Magnetization (M_y) as a function of X and Z (Region I).

The magnetic scalar potential is noted U_I in region I and U_{II} in region II. Notice that the magnetization given by Eq. (12) is divergence free $div\vec{M} = 0$. U_I and U_{II} are the solution of Laplace equation:

$$\Delta U_{I,II} = 0 \tag{13}$$

The general solution of the problem (13) without second member depend neither on the source of magnetic field nor on the magnetic formulation. In the absence of sources and in Cartesian coordinates, we must solve the Laplace equation in three dimensions, by considering the antiperiodic boundary conditions along the x and z coordinates, and the application of the variable separation method leads to the following form solutions for U_I and U_{II}

$$\begin{cases} U_I(x, y, z) = \displaystyle\sum_{n=1}^{\infty} \sum_{m=1}^{\infty} \left(A_{1,nm} e^{ky} + B_{1,nm} e^{-ky} \right) \cos(W_n x) \cos(W_m z) \\ U_{II}(x, y, z) = \displaystyle\sum_{n=1}^{\infty} \sum_{m=1}^{\infty} \left(A_{2,nm} e^{ky} + B_{2,nm} e^{-ky} \right) \cos(W_n x) \times \cos(W_m z) \end{cases} \tag{14}$$

with: $k = \sqrt{(W_m^2 + W_n^2)}$.

The unknown coefficients ($A_{1,nm}$, $B_{1,nm}$, $A_{2,nm}$, and $B_{2,nm}$) are determined using boundary and interface conditions (Figure 5):

- at $y = 0$ and $y = h_t$: The Condition (7) requires the magnetic field lines to penetrate orthogonally to the surface between the two media. The tangential magnetic field components H_x and H_z are zero (iron boundaries). This leads to:

$$\begin{cases} (A_{1,nm} + B_{1,nm}) = 0 \\ \left(A_{2,nm}e^{kh_t} + B_{2,nm}e^{-kh_t}\right) = 0 \end{cases} \tag{15}$$

- at $y = b$: Interface conditions between domains I and II knowing that the two domains I and II have the same relative permeability ($\mu_r = 1$), we impose the conditions of continuity of the normal flux density (B_y) and the tangential field (H_x and H_z) at $y = b$ defined as follows:

$$\begin{cases} B_{Iy}\,|_{y=b} = B_{IIy}\,|_{y=b} \Rightarrow H_{Iy} + M_y\,|_{y=b} = H_{IIy}\,|_{y=b} \\ H_{Ix} = H_{IIx}\,|_{y=b} \\ H_{Iz} = H_{IIz}\,|_{y=b} \end{cases} \tag{16}$$

The coefficients are determined after solving an algebraic system of linear equations arising from Eqs. (15) and (16).

In the same way, the method is applied to the field calculation created by the upper magnet inductor (the lower inductor magnets are off), and the solution of the scalar potential U_{III} in domain III (magnet region) and U_{IV} in domain IV (air region) are given as follows,

$$\begin{cases} U_{III}(x,y,z) = \displaystyle\sum_{n=1}^{\infty}\sum_{m=1}^{\infty}\left(A_{3,nm}e^{ky} + B_{3,nm}e^{-ky}\right) \times \cos(W_n x) \times \cos(W_m z) \\ U_{IV}(x,y,z) = \displaystyle\sum_{n=1}^{\infty}\sum_{m=1}^{\infty}\left(A_{4,nm}e^{ky} + B_{4,nm}e^{-ky}\right) \times \cos(W_n x) \times \cos(W_m z) \end{cases} \tag{17}$$

The coefficients $A_{3,nm}$, $B_{3,nm}$, $A_{4,nm}$, and $B_{4,nm}$ are determined using boundary conditions and the interface along the y-axis. At $y = 0$ and $y = h_t$, we use the same condition cited in Eq. (7) which leads to:

$$\begin{cases} (A_{3,nm} + B_{3,nm}) = 0 \\ \left(A_{4,nm}e^{kh_t} + B_{4,nm}e^{-kh_t}\right) = 0 \end{cases} \tag{18}$$

Domains III and IV have the same magnetic permeability ($\mu_r = 1$), so the normal flux density (B_y) and tangential magnetic fields (H_x and H_z) will be equal at $y = h_t - h$. The two following expressions arise:

$$\begin{cases} B_{IIIy}\,|_{y=h_t-h} = B_{IVy}\,|_{y=h_t-h} \\ \qquad\qquad \Rightarrow H_{IIIy} + M\,|_{y=h_t-h} = H_{IVy}\,|_{y=h_t-h} \\ H_{IIIx} = H_{IVx}\,|_{y=h_{t_t}-h} \\ H_{IIIz} = H_{IVz}\,|_{y=h_t-h} \end{cases} \tag{19}$$

2.3.1. Induced Currents Density and Induced Power Expressions

The magnetic fields are directly linked to the expressions of the scalar magnetic potential (17) and (14) previously calculated in the different domains.

$$\begin{cases} \vec{H} = -g\vec{r}ad\Phi \\ \vec{B} = \mu\vec{H} + \vec{B}_r \end{cases} \tag{20}$$

The magnetic field created by the lower inductor in region (II) is defined as follows:

$$\vec{H}_{II} = H_{IIx}\vec{u}_x + H_{IIy}\vec{u}_y + H_{IIz}\vec{u}_z \tag{21}$$

with

$$\begin{cases} H_{IIx}(x,y,z) = \displaystyle\sum_{n=1}^{\infty}\sum_{m=1}^{\infty} W_n \times \left(A_{2,nm}e^{ky} + B_{2,nm}e^{-ky}\right) \times \sin(W_n x) \times \cos(W_m z) \\ H_{IIy}(x,y,z) = \displaystyle\sum_{n=1}^{\infty}\sum_{m=1}^{\infty} k \times \left(B_{2nm}e^{-ky} - A_{2,nm}e^{ky}\right) \times \cos(W_n x) \times \cos(W_m z) \\ H_{IIz}(x,y,z) = \displaystyle\sum_{n=1}^{\infty}\sum_{m=1}^{\infty} W_m \left(A_{2,nm}e^{ky} + B_{2,nm}e^{-ky}\right) \times \cos(W_n x) \times \sin(W_m z) \end{cases}$$

The magnetic field created by the upper inductor in the region (IV) is defined as follows:

$$\vec{H}_{IV} = H_{IVx}\vec{u}_x + H_{IVy}\vec{u}_y + H_{IVz}\vec{u}_z$$

$$\begin{cases} H_{IVx}(x,y,z) = \sum_{n=1}^{\infty}\sum_{m=1}^{\infty} W_n \times \left(A_{4,nm}e^{ky} + B_{4,nm}e^{-ky}\right) \times \sin(W_n x) \times \cos(W_m z) \\ H_{IVy}(x,y,z) = \sum_{n=1}^{\infty}\sum_{m=1}^{\infty} k \times \left(B_{4,nm}e^{-ky} - A_{4,nm}e^{ky}\right) \times \cos(W_n x) \times \cos(W_m z) \\ H_{IVz}(x,y,z) = \sum_{n=1}^{\infty}\sum_{m=1}^{\infty} W_m \left(A_{4,nm}e^{ky} + B_{4,nm}e^{-ky}\right) \times \cos(W_n x) \times \sin(W_m z) \end{cases} \quad (22)$$

By applying the principle of superposition, the total magnetic flux density created in the air separating the two inductors (magnets) is given as follows:

$$\vec{B} = \mu_0\left(\vec{H}_{II} + \vec{H}_{IV}\right) = B_x\vec{u}_x + B_y\vec{u}_y + B_z\vec{u}_z$$

$$\begin{cases} B_x(x,y,z) = \sum_{n=1}^{\infty}\sum_{m=1}^{\infty} \mu_0 W_n \times \left(\left(\left(A_{24,nm})e^{ky}\right) + (B_{24,nm})\, e^{-ky}\right)\right) \times \sin(W_n x) \times \cos(W_m z) \\ B_y(x,y,z) = \sum_{n=1}^{\infty}\sum_{m=1}^{\infty} k\mu_0 \times \left((-A_{24,nm})\, e^{ky} + (B_{24nm})\, e^{-ky}\right) \times \cos(W_n x) \times \cos(W_m z) \\ B_z(x,y,z) = \sum_{n=1}^{\infty}\sum_{m=1}^{\infty} \mu_0 W_m \times \left(\left(\left(A_{24,nm})e^{ky}\right) + (B_{24,nm})\, e^{-ky}\right)\right) \times \cos(W_n x) \times \sin(W_m z) \end{cases} \quad (23)$$

with: $\begin{cases} A_{24,nm} = A_{2,nm} + A_{4,nm} \\ B_{24,nm} = B_{2,nm} + B_{4,nm} \end{cases}$.

To obtain a homogeneous distribution of the temperature in the plate, its velocity should be low (typically 1 m/s). Hence, the reaction field due to the induced currents in the plate can be neglected. The eddy currents in the conducting plate are then computed using:

$$r\vec{o}t\vec{J} = -\sigma\frac{\partial\vec{B}}{\partial t} \quad (24)$$

$$\begin{cases} \frac{\partial J_z}{\partial y} = \sigma V\frac{\partial B_x}{\partial x} \\ \frac{\partial J_x}{\partial y} = -\sigma V\frac{\partial B_z}{\partial x} \end{cases} \quad (25)$$

where σ is the electric conductivity of the workpiece, and $V = \frac{\partial x}{\partial t}$ is the speed of movement of the conductive workpiece.

After development, the induced current density components (along the x and y directions) in the conductive workpiece are obtained as follows:

$$\begin{cases} J_z(x,y,z) = \sum_{n=1}^{\infty}\sum_{m=1}^{\infty} \frac{\sigma\mu_0\,(W_n)^2}{k} \times \left(\left(\left(A_{24,nm})e^{ky}\right) - (B_{24,nm})\, e^{-ky}\right)\right) \times \cos(W_n x) \times \cos(W_m z) \\ J_x(x,y,z) = \sum_{n=1}^{\infty}\sum_{m=1}^{\infty} \frac{k\mu_0 W_n W_m}{k} \times \left(\left(\left(A_{24,nm})e^{ky}\right) - (B_{24,nm})\, e^{-ky}\right)\right) \times \sin(W_n x) \times \sin(W_m z) \end{cases} \quad (26)$$

Resulting power loss density using the 3D model is obtained as:

$$p\,(x,y,z) = \frac{1}{\sigma}((J_x(x,y,z))^2 + (J_z(x,y,z))^2) \quad (27)$$

The total heating power dissipated by Joule effect in the plate is computed by the integration of the power density in the volume of the plate:

$$p_T = \int_{-L/2}^{L/2} \int_{-y_1}^{y_1} \int_{-z_p/2}^{z_p/2} \left(\frac{1}{\sigma} (J_x(x,y,z)^2 + J_z(x,y,z)^2) \right) dxdydz \tag{28}$$

where z_p is the transversal length of the workpiece.

3. 3D TRANSIENT THERMAL ANALYSIS MODEL

3.1. 3D Thermal Problem Definition

The spatiotemporal distribution of temperature inside the conductive workpiece, subjected to a motion at constant speed, is governed by the following equation:

$$\rho c_p \left(\frac{\partial T}{\partial t} + \vec{v} \cdot \vec{grad} T \right) = \lambda \Delta T + p\,(x,y,z,t) \tag{29}$$

where $\vec{v} \cdot \vec{grad} T$ is the convective term due to the movement of the workpiece. The convective term due to the movement makes the analytical resolution of the thermal diffusion Equation (29) difficult. For simplifying the study, we assume in all what follows that the thermal source is mobile, and the plate to be heated is fixed. For this, a change of reference frame is performed ($x = x - V \cdot t$). The result is the annulment of convective term in Eq. (29). Note that the transient thermal problem is limited in the heating box containing the conductive workpiece and the surrounding air as shown in Figure 7.

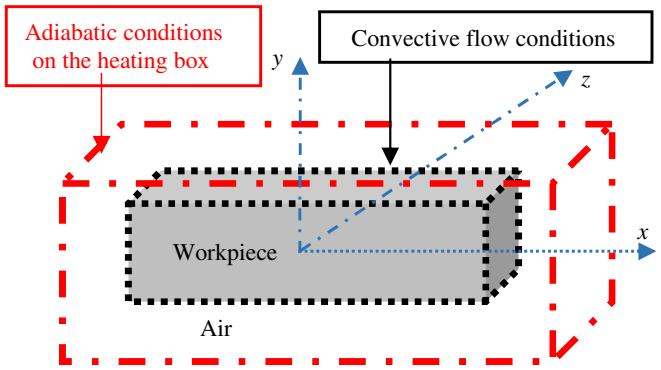

Figure 7. Geometric model of the thermal problem in 3D.

In Cartesian coordinates, the 3D thermal problem is written as the following system:

$$\begin{cases} \dfrac{\partial T}{\partial t} = a \left(\dfrac{\partial^2 T}{\partial^2 x} + \dfrac{\partial^2 T}{\partial^2 y} + \dfrac{\partial^2 T}{\partial^2 z} \right) + p\,(x,y,z,t)) \\ \dfrac{\partial T}{\partial x} = h_X (T - T_{X\infty}), \quad (x = L/2, \quad x = -L/2) \\ \dfrac{\partial T}{\partial y} = h_y (T - T_{y\infty}), \quad (y = y_1, \quad y = -y_1) \\ \dfrac{\partial T}{\partial z} = h_z (T - T_{z\infty}), \quad (z = z_1/2, \quad z = -z_1/2) \\ T(x,y,z,t=0) = f(x,y,z) = T_0 \end{cases} \tag{30}$$

This is the heat diffusion equation in transient state that we will solve analytically by using the Green's functions method.

In Eq. (30), $p(x,y,z,t)$ denotes the internal volumetric losses density given by Eq. (27); $\lambda(T)$, $\rho(T)$, and $c_p(T)$ denote respectively the thermal conductivity, specific mass, and specific heat; T_0 and T_∞ are

respectively the initial workpiece temperature and airgap temperature; h_x, h_y, and h_z represent the heat exchange coefficients in the different directions.

The thermal diffusivity a is defined as:

$$a(T) = \frac{\lambda(T)}{\rho(T)c_p(T)}$$

3.2. Analytical Expression of the Temperature

For solving the system Equation (30) we focused on the new particular analytical method, employing Green's functions. This method is based on the following steps:

- Determine a solution in the form of a linear combination of own functions;
- Determine the constants by the methods of orthogonal functions (initial conditions);
- Calculate the corresponding Green function to the homogeneous solution;
- Determine the corresponding Green function to the general solution;
- Calculate the general solution of the thermal problem.

The general solution of Eq. (30) in the whole domain Ω of the part can be represented in terms of the Green's function, by the following expression [25]:

$$\begin{aligned} T(M,t) = & \int_{\Omega} f(M')G(M,t/M',t'=0)d\Omega' + \frac{a}{\lambda}\int_0^t dt' \int_{\Omega} P(M,t/M',t')G(M,t/M',t')d\Omega \\ & + a\int_0^t dt' \sum_i \iint_{si} \left[\frac{f(M_i',t')G(M,t/M_i',t')}{\lambda}\right] ds_i' a\int_0^t dt' \sum_i \iint_{si} \\ & \left[-T(M_i',t')\frac{\partial G(M,t/M_i',t')}{\partial n_i'}\right] ds_i' \end{aligned} \tag{31}$$

with M, M' denoting the points in space defined respectively by the coordinates (x, y, z) and (x', y', z'), G the Green's function, and $p(M, t/M', t')$ the heat source. Equation (31) has four terms, where the first term represents the homogeneous solution; the second term defines the particular solution; the third and fourth present respectively prescribed heat flux and prescribed temperature at the extern surface of the workpiece; G is the Green function of general solution associated with the thermal problem defined in [25] as:

$$\begin{aligned} G_{nmq}(x,y,z,t/x',y',z',t') = & \frac{1}{2Ly_1z_p} + \sum_{n=1}^{\infty}\sum_{m=1}^{\infty}\sum_{q=1}^{\infty} \frac{4}{Ly_1z_1}\cos\left(\frac{2n\pi}{L}x'\right) \\ & \times \cos\left(\frac{2n\pi}{L}x\right)\cos\left(\frac{m\pi}{y_1}y'\right)\cos\left(\frac{2q\pi}{z_1}z'\right)\cos\left(\frac{m\pi}{y_1}y\right)\cos\left(\frac{2q\pi}{z_1}z\right) \\ & \times \left(\exp\left(-a\left(\left(\frac{2n\pi}{L}\right)^2 + \left(\frac{m\pi}{y_1}\right)^2 + \left(\frac{2q\pi}{z_1}\right)^2\right)(t-t')\right)\right) \end{aligned} \tag{32}$$

Using the previous Green function (32), the general solution of the problem is computed by Equation (31). The 3D spatiotemporal profile of the temperature inside the workpiece is given as:

$$T(x,y,z,t) = T_h(x,y,z,t) + T_p(x,y,z,t) + c_3\left(\frac{h_xT_{x\infty}}{L} + \frac{h_yT_{y\infty}}{2y_1} + \frac{h_zT_{z\infty}}{z_1}\right)t \tag{33}$$

More calculation details and expressions of thermal model are given in Appendix A [25].

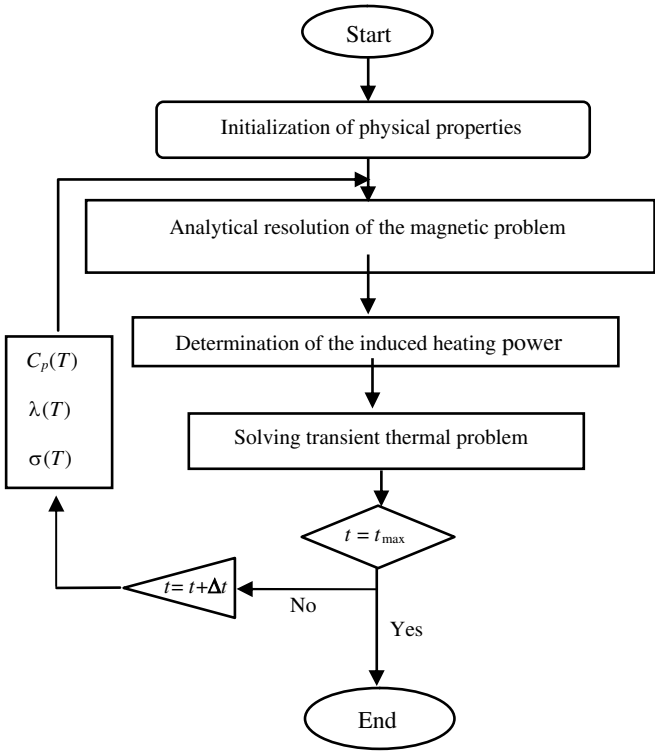

Figure 8. Flowchart solving magneto-thermal coupled problem.

3.3. Coupling of the 3D Electromagnetic and 3D Thermal Transiet Solutions

The organizational flowchart of the transient magneto-thermal coupling is illustrated in Figure 8.

The variation of the physical properties of the workpiece as a function of temperature is given by the following expressions.

$$\sigma(T) = \frac{\sigma_0}{1 + \alpha(T - T_0)} \tag{34}$$

for electrical conductivity;

$$\frac{\lambda}{\sigma} = L_0 T \tag{35}$$

for thermal conductivity;

$$C_p = \frac{E}{M_p \cdot \Delta T} \tag{36}$$

for the specific heat.

σ_0 is the conductivity at T_0°C (initial reference temperature); α is the temperature coefficient relative to the electrical conductivity; $L_0 = 2.45 * 10^{-8}$ is the constant of Lorentz; E and M_p represent respectively the energy stored and the mass of the workpiece.

4. RESULTS AND VALIDATION

To show the applicability of the 3D models developed beforehand, the performances of a new permanent magnet linear induction heater as shown in Figure 1 is studied. For the topology, all the dimensions and properties of the materials are found in Table 1.

4.1. Electromagnetic Problem Results

We compare, in the following section, some results of the electromagnetic problem, obtained by the 3D, 2D, and quasi-3D magnetic analytical developed models with those obtained by the 3D finite element model.

The distribution of the flux density component B_y along the longitudinal coordinate x in the surface of the workpiece ($y = y_1$) at $z = 0$ is illustrated in Figure 9(a), noting that the B_y values obtained by the different 2D and 3D analytical and numerical models are in a good agreement. This component of the induction presents a periodic variation in this direction with amplitude of 0.57 T.

On the other hand, at $z = z_p/2$, the paces of the flux density component B_y according to the longitudinal coordinate x at $y = 0$ and $y = y_1$, illustrated in Figures 9(b) and 10 successively are obtained by the 3D analytical model and compared only to the 3D FEM because this line is not located in the two-dimensional plane (x, y) of the 2D analytical and numerical models developed in [25]. We note that this component of the induction presents a periodic variation in this direction, but the amplitude decreases considerably (0.57 T at $z = 0$ and $y = y_1$ to 0.27 T at $y = y_1$ and $z = z_p/2$).

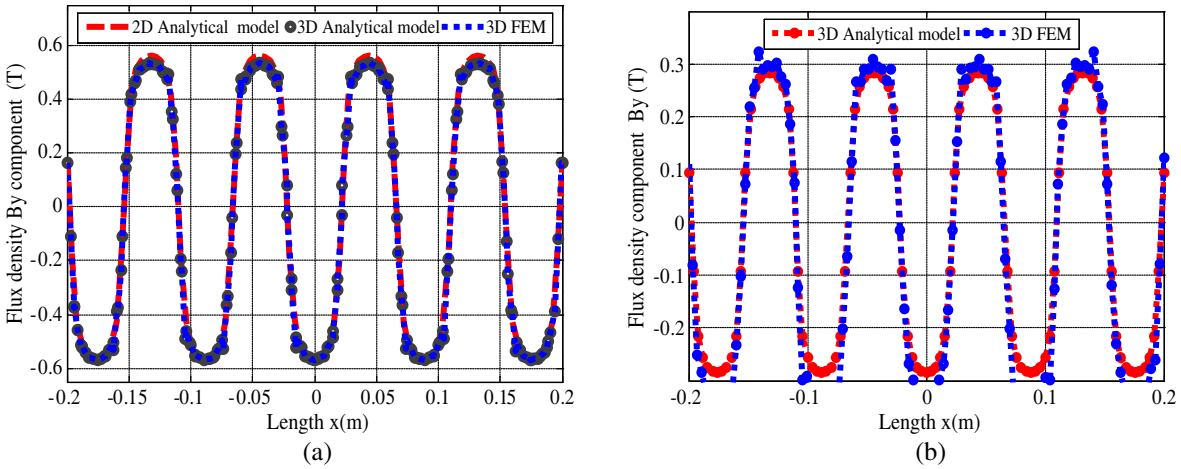

Figure 9. Flux density B_y component: (a) B_y versus longitudinal coordinate x at ($y = y_1$) the surface of the workpiece and $z = 0$, (B) B_y versus longitudinal coordinate x at ($y = y_1$ and $z = z_1/2$).

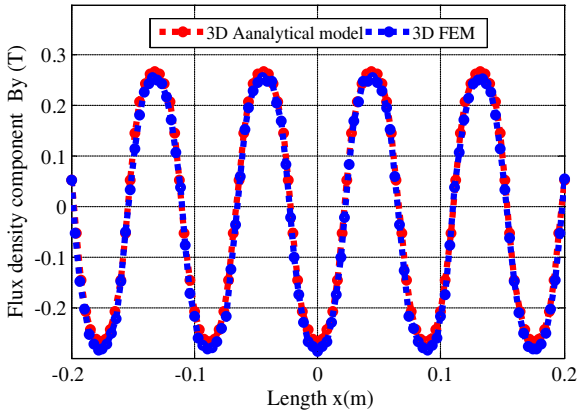

Figure 10. Flux density component B_y versus longitudinal coordinate X at ($y = 0$ and $z = z_1/2$).

Figures 11(a) and 11(b) show respectively the spatial distribution of the flux density component B_y versus the transversal coordinate z at $x = a + e_g$ (under a South pole) and $x = 0$ (under a north pole) for $y = y_1$. We observe that the flux density component (B_y) remains constant (approximately

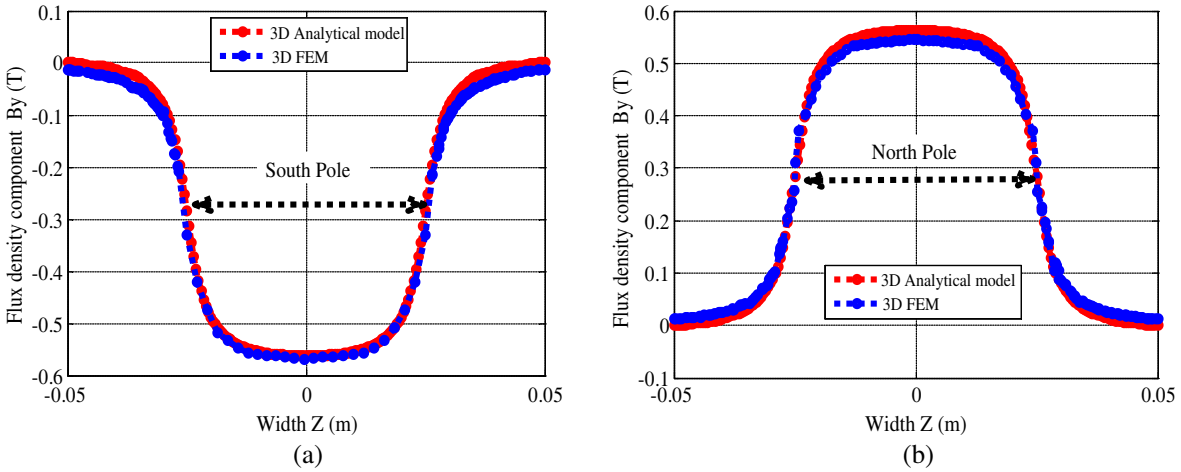

Figure 11. Flux density component B_y: (a) B_y versus z-direction at $y = y_1$ and $x = a + e_g$ (South pole), B_y versus z-direction at $y = y_1$ and $x = 0$ (North pole).

0.56 T) on a level and collapses by 50% at the ends of the workpiece (0.27 T at $z = z_p/2$ or $z = -z_p/2$) and is canceled at a distance from $z = z_p$ or $-z_p$).

Figures 12(a), (b) and Figures 13(a), (b) illustrate respectively the evolution of the induced currents density components (J_z and J_x) versus x-direction in the surface and the center of the workpiece at $z = 0$ for J_z and $z = z_1/2$ for J_x for a linear speed $V_{\max} = 1.2\,\text{m/s}$. We observe that these components present a periodic variation in this direction with amplitudes ($J_z = 2.10^7\,\text{A/m}^2$ and $J_x = 1.3.10^7\,\text{A/m}^2$) at the surface of the workpiece, and they remain relatively large ($J_z = 1.8.10^7\,\text{A/m}^2$ and $J_x = 1.10^7\,\text{A/m}^2$) in the center.

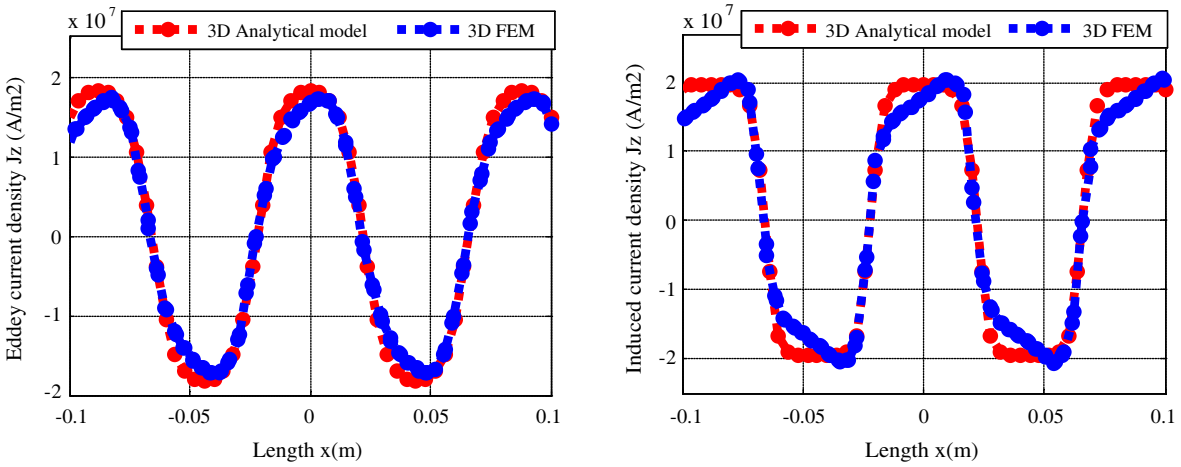

Figure 12. Induced current density component J_z in the conducting plate versus the x coordinate ($z = 0$, Velocity $= 1.2\,\text{m/s}$): (a) in the middle ($y = 0$), (b) in the surface ($y = y_1$).

In Figures 14(a), (b) respectively, the distribution of the induced current component J_z along the coordinate z at the surface ($y = y_1$) and at the center ($y = 0$) of the piece for ($x = 0$) is shown. We note that the current density J_z has a maximum value (approximately $19.5\,\text{A/mm}^2$) at the surface of the part and ($18.2\,\text{A/mm}^2$) at the center of the part. It collapses by 50% at the ends of the workpiece Figures 15(a) and (b).

Figures 16(a) and (b) respectively show the distribution of the induced current component J_x along

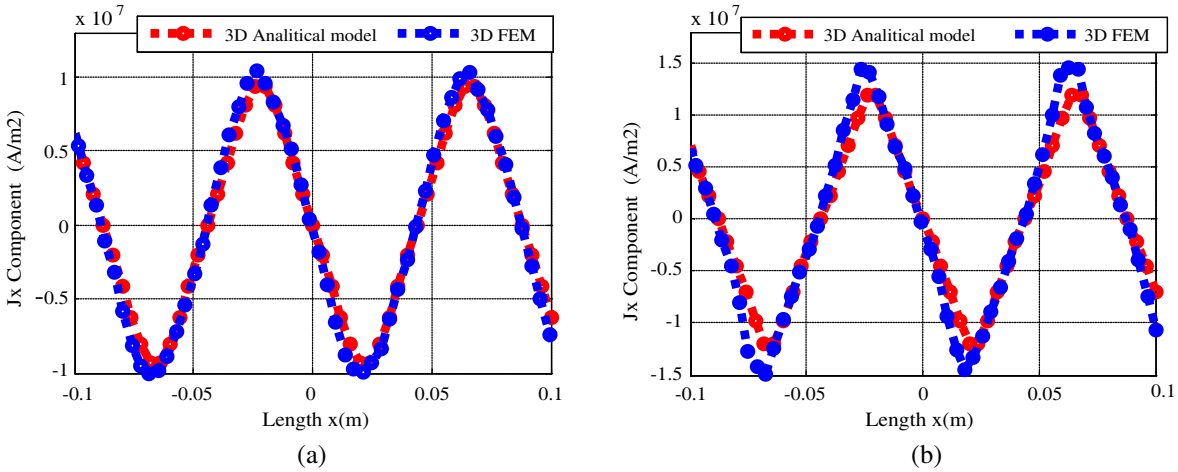

Figure 13. Induced current density component J_x in the conducting plate versus the x coordinate ($z = z_1/2$, Velocity $= 1.2\,\mathrm{m/s}$): (a) in the middle ($y = 0$), (b) in the surface ($y = y_1$).

the coordinate z at the surface and at the center ($y = 0$) of the workpiece ($v = 1.2\,\mathrm{m/s}$). We notice that the component J_x is maximum at the ends of the part ($z = z_p/2$ and $z = -z_p/2$) and cancels out at $z = 0$. These remarks are valid whatever the values of x and y, as shown in Figures 17(a) and (b).

Figure 18 illustrates the variation patterns of the total heating power, induced in the workpiece as a function of the speed, obtained by all the analytical and numerical models (2D and 3D). It is clearly shown that the analytical model developed in 3D gives a better estimate of the heating power. The comparison, given in Table 2, of the results obtained by the 3D analytical model with those given by the 3D FEM model shows a better agreement than those obtained by the all 2D models.

Table 2. Total heating power obtained by the different models.

Motion (m/s)	**Total induced heating power (W)**				
	Analytical 2D	***FEM 2D***	***Analytical Corrected 2D***	***FEM 3D***	***Analytical 3D***
0.2	82.95	82.43	35.49	32.65	33.19
0.4	328.45	328.22	156.39	130.46	132.79
0.6	726.77	726.15	346,10	293	298.78
0.8	1262,7	1262	601,46	519.6	531.16
1	1917,2	1916.4	913.44	809.7	829.94
1.2	2668,6	2668	1271.9	1061	1195.1
1.4	3494,5	3493	1666.1	1472,4	1626.7

From Figure 19(b), we note that the relative difference between the results obtained by the 3D analytical and finite element models is around 1.63% at a translation speed $v = 0.2\,\mathrm{m/s}$. It remains small when the speed increases (around 2.18% for $v = 0.8\,\mathrm{m/s}$), but the relative difference of the 2D models shown in Figure 19(a) reaches 142% at $v = 0.8\,\mathrm{m/s}$. Note that for the same speed ($v = 0.8\,\mathrm{m/s}$) the difference obtained by the corrected-2D analytical model is 8% [25]. We also note that for speeds higher than 1 m/s, the error can become relatively important. Besides it passes from 2.18% for a speed $V = 0.8\,\mathrm{m/s}$ to 13% for a speed $V = 1.2\,\mathrm{m/s}$.

As shown in Figure 18, the developed analytical 3D magnetic model gives better results in the estimation of the total induced heating power using Equation (28). Obviously, these results are

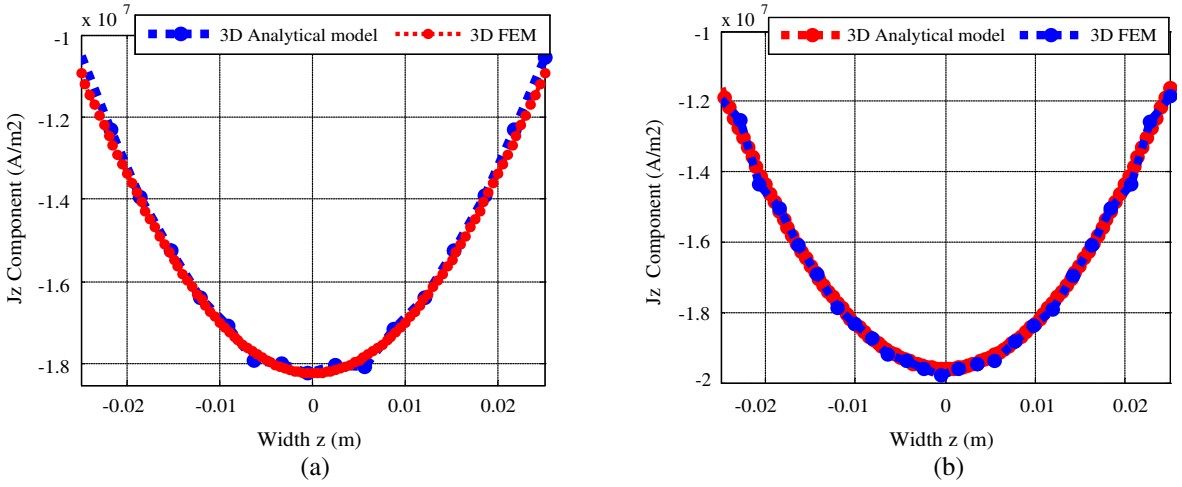

Figure 14. Induced Current density Component J_z in the conducting plate versus the z coordinate ($x = 0$, Velocity= 1.2 m/s): (a) in the middle ($y = 0$), (b) in the surface ($y = y_1$).

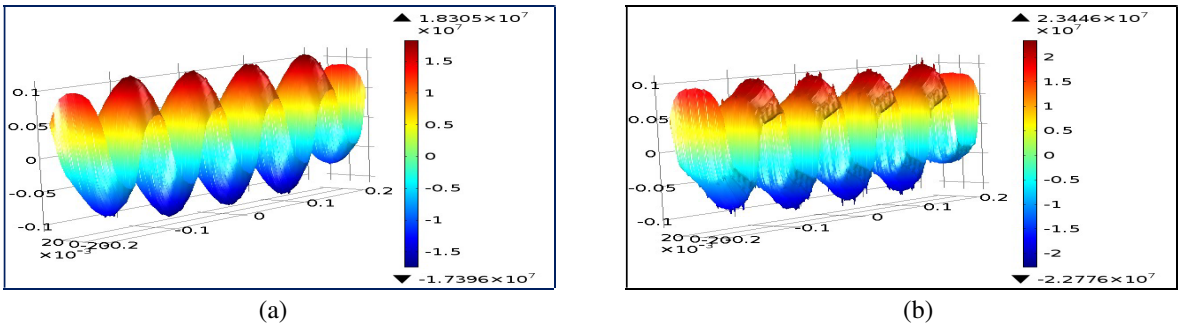

Figure 15. Distribution of J_z Induced Current density Component in the x-z plane ($v = 1.2$ m/s): (a) in the middle of the workpiece, (b) in the surface ($y = y_1$).

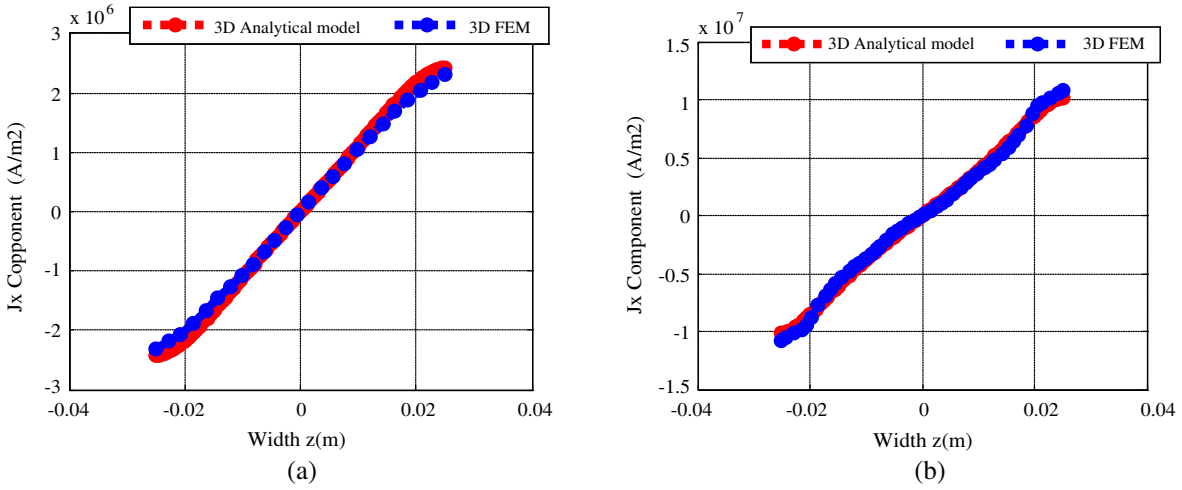

Figure 16. Induced Current density Component J_x in the conducting plate versus the z coordinate ($x = 0$, Velocity = 1.2 m/s): (a) in the middle ($y = 0$), (b) in the surface ($y = y_1$).

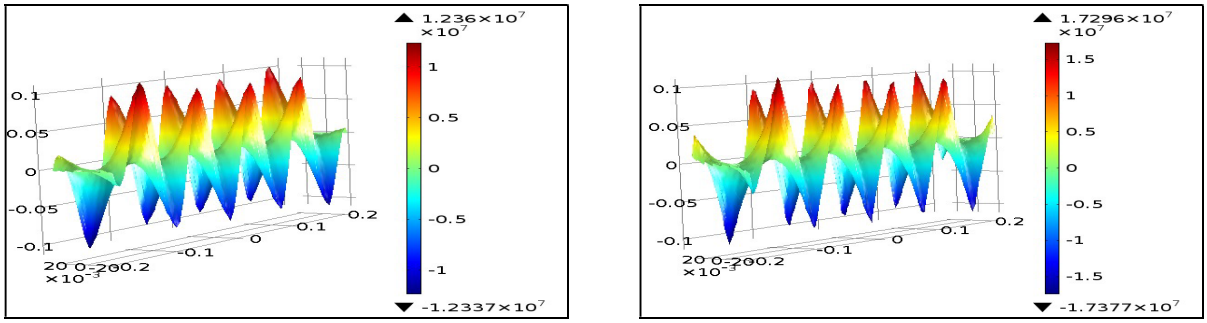

(a) (b)

Figure 17. Distribution of J_x Induced Current density Component in the x-z plane ($v = 1.2\,\mathrm{m/s}$): (a) in the middle of the workpiece, (b) in the surface ($y = y_1$).

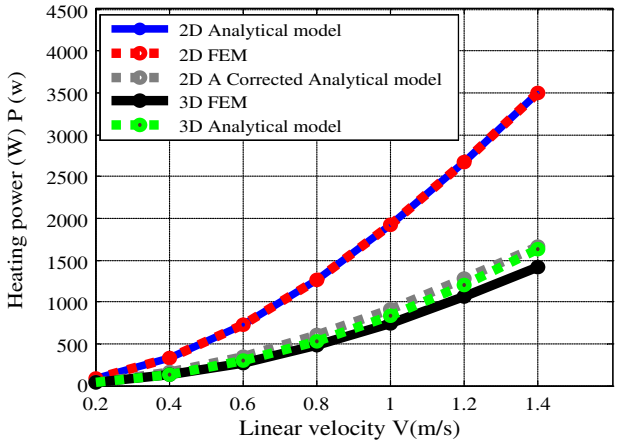

Figure 18. Total induced heating power versus constant translation velocity.

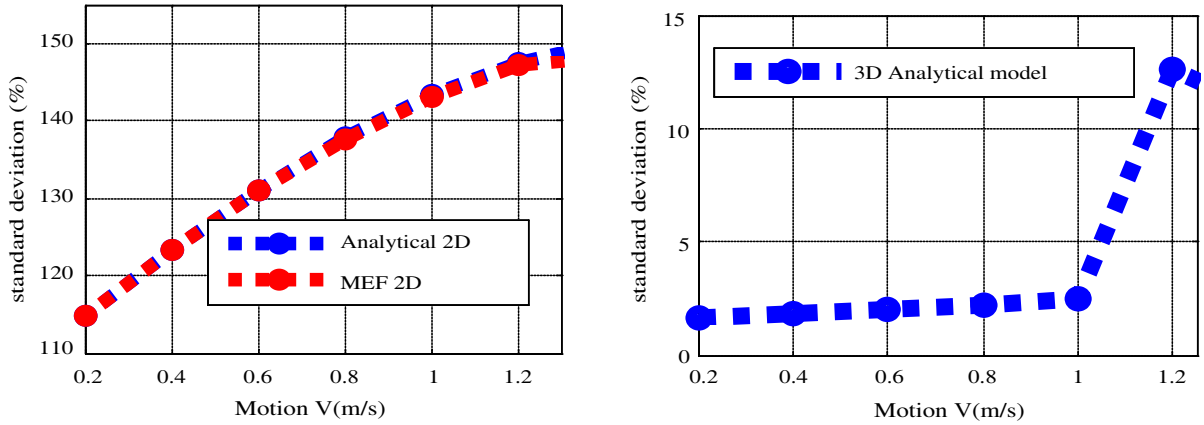

(a) (b)

Figure 19. Difference in (%) between the total heating power obtained by different models as a function of the speed: (a) 2D MEF and 2D Analytical compared to FEM 3D, (b) 3D Analytical compared to that obtained by FEM 3D.

consistent with those obtained by the 3D finite element model. The latter is implemented in software finite elements. To perform 3D finite element calculations, a 3D mesh of 360 140 tetrahedral elements leading to the resolution of a global algebraic system having 2287999 degrees of freedom is used. Obviously, the 3D models take into account all the longitudinal edge effects, which are not fully taken into account in the analytical model. The computation time in 3D FEM using a workstation (4 GB of RAM, Intel® Core^{TM} processor i5-4258U) is 960 s, while the computation time of the proposed analytical model is about 1(s).

4.2. Thermal Results and Experimental Comparison

The 3D transient thermal study of the induction heating device shown in Figure 1 is approached in this part using the developed 3D analytical magneto-thermal model with the coupling approach illustrated in Figure 8. The two expressions of the heating power density source given by Eqs. (4) and (27) and derived respectively with 2D-extended-3D and 3D models are considered in this study. They are noted by P_1 for the power calculated by the 3D analytical model and P_2 when the power is calculated by the corrected 2D analytical model.

Noting that all the physical parameters of the piece $\lambda(T)$, $\rho(T)$ and $c_p(T)$ are dependent on temperature, and the values of these parameters corresponding to the initial temperature are shown in Table 1. $T_0 = 25°C$ is the initial value of temperature inside the workpiece, and $T_{ex} = 25°C$ is the initial air-gap temperature.

This study is limited in the heating box constituting the conductive workpiece and the surrounding air. The boundary conditions adopted are of the Neumann type, considering that the convective heat flow is mainly directed along y and z.

The time evolution of the temperature at the center of the workpiece obtained by this approach is illustrated in Figure 20. Compared to 2D-extended-3D model, the developed transient 3D nonlinear thermal model gives better and very accurate results of temperature evaluation. The results obtained by this model have a very good agreement with those obtained by the 3D FEM model. The calculation time by the proposed transient nonlinear analytical model is approximately 21.90 s using the workstation (4 GB RAM, Intel® Core^{TM} i5-4258U processor), while the calculation of nonlinear 3D FEM is tens of minutes.

To validate the developed 3D magnetothermal analytical model, a prototype of transverse flux induction heating made and described in [13] is used, where a view of the experimental set is shown.

The heating demonstrator includes two inductors with permanent magnets (halbach configuration). The part to be heated has a length of 200 mm, width of 50 mm, and thickness of 15 mm. It is placed between these two inductors. This piece is subjected to an alternating linear movement. The movement creates induced currents that dissipate heating power by Joule effect.

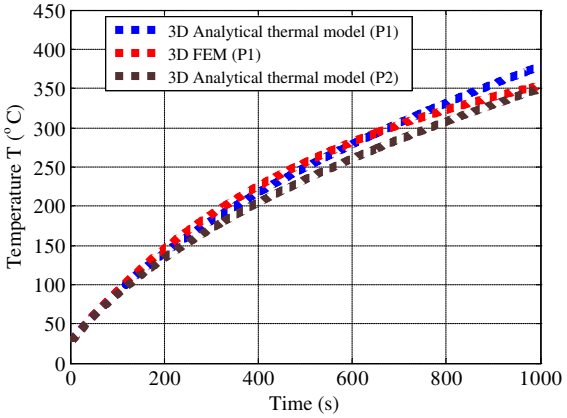

Figure 20. Temperature evolution evaluated at the center of de workpiece ($x = 0$, $y = 0$, $z = 0$, $V = 1.2$ m/s.

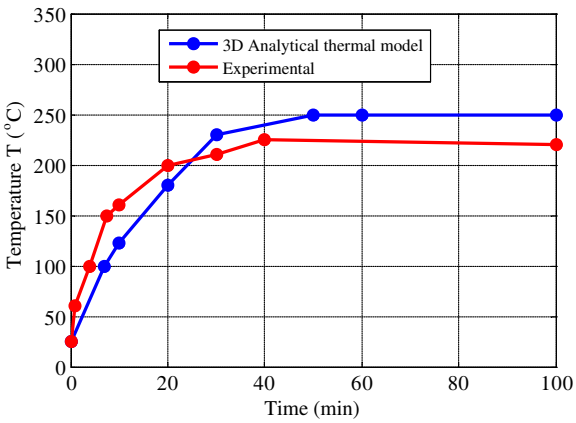

Figure 21. Temperature evolution evaluated at the surface of the workpiece at ($x = 0$, $y = y_1$, $z = 0$) with $V = 1.18$ m/s.

Figure 21 shows the evolution of temperature over time at the surface of the workpiece. It can be seen that the temperature at the surface of the workpiece is 238°C after 40 minutes (225°C measured experimentally [13]) and remains relatively constant about 250°C after 100 min of heating process (230°C measured experimentally). In fact, the temperature of the magnets reaches 90°C at 50 min, which causes a substantial decrease of their remanence and consequently the decrease of the heating power density. It is important to note that the decrease of the permanent magnet remanence versus temperature has been taken into account in the 3D analytical model. One can observe that the results obtained by the analytical model agree with the experimental measurements in [13].

5. CONCLUSION

In fact, there is no exact 3-D analytical calculation of coupling magnetic and thermal problems in electrical machines using formal resolution of Maxwell and heat equations.

In this paper, we have proposed a new 3D transient analytical model to analyze coupled magneto-thermal phenomena in transverse flux induction heating devices.

First, an exact 3D analytical magnetic model is developed, so that the heating power can be rapidly evaluated.

Besides, a new thermal analytical model based on the synergy between the variables' separation method and the analysis method of transient regimes by the Green functions is developed. The latter, coupled with the 3D magnetic model, allows a very accurate simulation of nonlinear and transient magneto-thermal phenomenon.

The models obtained are finally applied to a PM transverse flux induction heating device. The magneto-thermal results are in agreement with those obtained using a finite elements method. Therefore, the developed magneto-thermal model presents a fast and accurate tool for the design of induction heating devices.

APPENDIX A.

Equation (33) has three terms, where the first term represents the homogeneous solution, calculated as:

$$\begin{aligned} T_h(x,y,z,t) \;=\; & \frac{1}{2Ly_1z_p}\int_{x'}\int_{y'}\int_{z'} f\left(x',y',z'\right)dx'dy'dz' \\ & +\sum_{n=1}^{\infty}\sum_{m=1}^{\infty}\sum_{q=1}^{\infty}\left[\begin{array}{l} \dfrac{4}{Ly_1z_p}\int_{x'}\int_{y'}\int_{z'} f(x',y',z')\cos(\dfrac{2n\pi}{L}x') \\ \cos\left(\dfrac{m\pi}{y_1}y'\right)\cos(\dfrac{2q\pi}{z_1}z')dx'dy'dz' \\ \cos\left(\dfrac{2n\pi}{L}x\right)\cos\left(\dfrac{m\pi}{y_1}y\right)\cos\left(\dfrac{2q\pi}{z_1}z\right) \\ \exp\left(-a\left(\left(\dfrac{2n\pi}{L}\right)^2+(\dfrac{m\pi}{y_1}\right)^2+\left(\dfrac{2q\pi}{z_1}\right)^2\right)t\right) \end{array}\right] \end{aligned} \tag{A1}$$

with:

$$f(x,y,z) = T(x,y,z,t=0) = T_0,\ \text{Temperature workpiece at } t=0.$$

The second term defines the particular solution, calculated as follows:

$$T_p(x,y,z,t) = \int_0^t\int_{-L/2}^{L/2}\int_{-y_1}^{-y_1}\int_{-z_1}^{z1} G_{nmq}(x,y,z,t/x',y',z',t')\times P(x',y',z',t')a2 \tag{A2}$$

$G_{nmq}(x,y,z,t/x',y',z',t')$ is the Green's function defined by Equation (32), and for more details on the computation of G see [28]. $p\left(x',y',z',t'\right)$ is the resulting power loss density obtained by the 3D magnetic model and defined by Equation (27).

The third of Equation (33) presents the heat flux exchanged by the different surfaces of the workpiece with the external environment, calculated with:

$$a\int_0^t dt' \sum_i \iint_{si} \left[\frac{f(M_i',t')G(M,t/M_i',t')}{\lambda}\right] ds_i' = c_3\left(\frac{h_x T_{x\infty}}{L} + \frac{h_y T_{y\infty}}{2y_1} + \frac{h_z T_{z\infty}}{z_1}\right) t \tag{A3}$$

REFERENCES

1. Lucía, Ó., P. Maussion, E. J. Dede, and J. M. Burdío, "Induction heating technology and its applications: Past developments, current technology, and future challenges," *IEEE Trans. Ind. Electron.*, Vol. 61, No. 5, 2509–2520, May 2014.
2. Mach, F., V. Starman, P. Karban, I. Dolezel, and P. Kus, "Finite element 2D model of induction heating of rotating billets in system of permanent magnets and its experimental verification," *IEEE Trans. Ind. Electron.*, Vol. 61, No. 5, 2584–2591, May 2014.
3. Mach, F., P. Karban, and I. Doležel, "Induction heating of cylindrical nonmagnetic ingots by rotation in static magnetic field generated by permanent magnets," *Journal of Computational and Applied Mathematics*, Vol. 236, No. 18, 4732–4744, ELSVIER, Dec. 2012.
4. Han, W., et al., "Commercial design and operating characteristics of a 300 kW superconducting induction heater (SIH) based on HTS magnets," *IEEE Trans. Appl. Supercond.*, Vol. 29, No. 5, 1–5, Aug. 2019.
5. Choi, J., et al., "Design and performance evaluation of a multi-purpose HTS DC induction heating machine for industrial applications," *IEEE Trans. Appl. Supercond.*, Vol. 25, No. 3, 1–5, Jun. 2015.
6. Lubin, T., D. Netter, J. Leveque, and A. Rezzoug, "Induction heating of aluminium billet subjected to a strong rotating magnetic field produced by superconducting windings," *IEEE Trans. Magn.*, Vol. 45, No. 5, 2118–2127, May 2009.
7. Choi, J., C.-K. Lee, S. Cho, M. Park, I.-K. Yu, and M. Iwakuma, "Recent development and research activities of induction heater with high-TC superconducting magnets for commercialization," *SN Appl. Sciences*, Vol. 1, No. 1, 59–64, 2018.
8. Abdi, A., Y. Ouazir, G. Barakat, and Y. Amara, "Permanent magnet linear induction heating device: Newtopology enhancing performances," *COMPEL*, Vol. 37, No. 5, 1755–1767(13), Oct. 2018.
9. Ammar, A., "2D hybrid magnetic model calculation in axisymmetric device," *Progress In Electromagnetics Research Letters*, Vol. 103, 15–23, 2022.
10. Fabbri, M., A. M. Forzan, S. Lupi, A. Morandi, and P. L. Ribani, "Experimental and numerical analysis of DC induction heating of aluminium billets," *IEEE Trans. Magn.*, Vol. 45, No. 1, 192–200, Jan. 2009.
11. Runde, M., N. Magnusson, C. Fulbier, and C. Buhrer, "Commercial induction heaters with high temperature superconductor coils," *IEEE Trans. Appl. Supercond.*, Vol. 21, No. 3, 1379–1383, 2011.
12. Mach, F., P. Karban, I. Doležel, P. Šíma, and Z. Jelíek, "Model of induction heating of rotating non-magnetic billets and its experimental verification," *IEEE Trans. Magn.*, Vol. 50, No. 2, 309–312, Feb. 26, 2014.
13. Bensaidane, H., T. Lubin, S. Mezani, Y. Ouazir, and A. Rezzoug, "A new topology for induction heating system with PM excitation: Electromagnetic model and experimental validations," *IEEE Trans. Magn.*, Vol. 51, No. 10, 3479–3487, Jun. 2015.
14. Qin, Z., H. Talleb, and Z. Ren, "A proper generalized decomposition-based solver for nonlinear magnetothermal problems," *IEEE Trans. Magn.*, Vol. 52, No. 1, 1–11, Oct. 2016.
15. Moro, F. and L. Codecasa, "A 3-D hybrid cell method for induction heating problems," *IEEE Trans. Magn.*, Vol. 53, No. 6, 1–4, Jun. 2017.
16. Ouazir, Y., A. Abdi, and H. Bensaidane, "2D analytical solution of transverse flux induction heating of the aluminum plates," *2012 XXth International Conference on Electrical Machines*, 2733–2738, Marseille, France, Sep. 2012.

17. Fabbri, M., A. M. Forzan, S. Lupi, A. Morandi, and P. L. Ribani, "Experimental and numerical analysis of DC induction heating of aluminium billets," *IEEE Trans. Magn.*, Vol. 45, No. 1, 192–200, Jan. 2009.
18. Aliferov, A., F. Dughiero, and M. Forzan, "Coupled magnetothermal FEM model of direct heating of ferromagnetic bended Tubes," *IEEE Trans. Magn.*, Vol. 46, No. 8, 3217–3220, Jul. 19, 2010.
19. D'Angelo, L. A. M. and H. De Gersem, "Quasi-3D finite-element method for simulating cylindrical induction-heating devices," *IEEE Trans. Magn.*, Vol. 2, 134–141, Aug. 2017.
20. Qin, Z., H. Talleb, and Z. Ren, "A proper generalized decomposition-based solver for nonlinear magnetothermal problems," *IEEE Trans. Magn.*, Vol. 52, No. 2, 1–9, Feb. 2016.
21. Ennassiri, H., G. Barakat, and Y. Amara, "Steady state hybrid thermal modelling of permanent magnet electrical machines," *Proc. Int. Conf. Ecol. Vehicles Renew. Energies (EVER)*, 1–6, 2016, doi: 10.1109/EVER.2016.7476420.
22. Zhu, S., M. Cheng, and X. Cai, "Direct coupling method for coupled field-circuit thermal model of electrical machines," *IEEE Trans. Magn.*, Vol. 33, No. 2, 473–482, Jun. 2018.
23. Nategh, S., O. Wallmark, M. Leksell, and S. Zhao, "Thermal analysis of a PMaSRM using partial FEA and lumped parameter modeling," *IEEE Trans. Energy Convers.*, Vol. 27, No. 2, 477–488, Jun. 2012.
24. Boughrara, K., F. Dubas, and R. Ibtiouen, "2-D exact analytical method for steady-state heat transfer prediction in rotating electrical machines," *IEEE Trans. Magn.*, Vol. 54, No. 9, 1–19, Sept. 2018.
25. Abdi, A., Y. Ouazir, G. Barakat, and Y. Amara, "Transient quasi-3D magneto-thermal analytical solution in PM induction heating device," *COMPEL — The International Journal for Computation and Mathematics in Electrical and Electronic Engineering*, Vol. 39 No. 5, 1131–1144, 2020, https://doi.org/10.1108/COMPEL-01-2020-0054.
26. Russell, R. L. and K. H. Norsworthy, "Eddy currents and wall losses inscreened-rotor induction motors," *Proceedings of the IEE Part A: Power Engineering*, Vol. 105, No. 20, 163, 1958.
27. Decreux, P. and G. Nicolas, "Finite length effects study in massive iron rotors using 3D electromagnetic field computation," *IEEE Trans. Magn.*, Vol. 31, No. 3, 2096–2099, May 1995.
28. De La Barriere, O., S. Hlioui, H. Ben Ahmed, et al., "3-D formal resolution ofMaxwell equations for the computation of the no load flux in an axial flux permanent magnet synchronous machine," *IEEE Trans. Magn.*, Vol. 48, No. 1, 128–136, 2012.
29. Pluk, K. J. W., T. A. van Beek, J. W. Jansen, and E. A. Lomonova, "Modeling and measurements on a finite rectangular conducting plate in an eddy current damper," *IEEE Trans. Industrial Electronics*, Vol. 61, No. 8, 4061–4072, Aug. 2014.
30. Paul, S., J. Wright, and J. Z. Bird, "3-D steady-state eddy current dampingand stiffness for a finite thickness conductive plate," *IEEE Trans. Magn.*, Vol. 50, No. 11, 6301404, Nov. 2014.
31. Jin, P., Y. Tian, Y. Lu, Y. Guo, G. Lei, and J. Zhu, "3-D analytical magnetic field analysis of the eddy current coupling with halbach magnets," *IEEE Trans. Magn.*, Vol. 56, No. 1, 1–4, Jan. 2020.
32. Lubin, T. and A. Rezzoug, "3-D analytical model for axial-flux eddy-current couplings and brakes under steady-state conditions," *IEEE Trans. Magn.*, Vol. 51, No. 10, 1–12, Oct. 2015.
33. Diriye, A., Y. Amara, and G. Barakat, "Three-dimensional modeling of permanents magnets synchronous machines using a 3D reluctance network," *2018 XIII International Conference on Electrical Machines (ICEM)*, 2304–2310, Alexandroupoli, Greece, Sep. 2018.
34. Jin, P., Y. Yuan, J. Minyi, F. Shuhua, L. Heyun, H. Yang, and S. L. Ho, "3-D analytical magnetic field analysis of axial flux permanent magnet machine," *IEEE Trans. Magn.*, Vol. 50, No. 11, 8103504, Nov. 2014.
35. Sahu, R., P. Pellerey, and K. Laskaris, "Eddy current loss model unifying the effects of reaction field and non-homogeneous 3-D magnetic field," *IEEE Trans. Magn.*, Vol. 56, No. 2, 1–4, Jan. 13, 2020.

36. Sun, X., S. Luo, L. Chen, R. Zhao, and Z. Yang, "Suspension force modeling and electromagnetic characteristics analysis of an interior bearingless permanent magnet synchronous motor," *Progress In Electromagnetics Research B*, Vol. 69, 31–45, 2016.
37. Verez, G., G. Barakat, and Y. Amara, "Influence of slots and rotor poles combinations on noise and vibrations of magnetic origins in 'U'-core flux-switching permanent magnet machines," *Progress In Electromagnetics Research B*, Vol. 61, 149–168, 2014.